applied optics

Analysis of single-mode fiber-optic extrinsic Fabry–Perot interferometric sensors with planar metal mirrors

Qiwen Sheng,[1] Guigen Liu,[1,2] Nezam Uddin,[1] and Ming Han[1,*]

[1]Department of Electrical and Computer Engineering, Michigan State University, East Lansing, Michigan 48824, USA
[2]Current address: Department of Radiology, Brigham & Women's Hospital, Harvard Medical School, Boston, Massachusetts 02115, USA
*Corresponding author: mhan@egr.msu.edu

Received 13 May 2021; revised 5 July 2021; accepted 4 August 2021; posted 6 August 2021 (Doc. ID 431364); published 2 September 2021

We theoretically study the spectral characteristics and noise performance of wavelength-interrogated fiber-optic sensors based on an extrinsic Fabry–Perot (FP) interferometer (EFPI) formed by thin metal mirrors. We develop a model and use it to analyze the effect of key sensor parameters on the visibility and spectral width of the sensors, including the beam width of the incident light, metal coating film thickness, FP cavity length, and wedge angle of the two mirrors. Through Monte Carlo simulations, we obtain an empirical equation that can be used to estimate the wavelength resolution from the visibility and spectral width, which can be used as a figure-of-merit that is inherent to the sensor and independent on the system noises. The work provides a useful tool for designing, constructing, and interrogating high-resolution fiber-optic EFPI sensors.

https://doi.org/10.1364/AO.431364

1. INTRODUCTION

Fiber-optic extrinsic Fabry–Perot (FP) interferometer (EFPI) sensors consisting of FP cavities fabricated at the tips of single-mode fibers (SMFs) have received increasing interest in measuring a wide range of parameters such as temperature [1–3], pressure [4], acoustic and ultrasonic waves [5,6], flow [7,8], refractive index [9], plasma radiation [10], and biochemical specifications [11,12], due to their simple structure, small size, and versatility in addition to many other advantages inherent to fiber-optic sensors. The parameters to be measured are encoded in the wavelength shift of the interferometric fringes in the reflection spectrum of the sensors, which are typically obtained using one of the three schemes: a laser whose wavelength is at the slope of the fringes along with a photodetector (intensity interrogation), a broadband source plus a spectrometer (angular interrogation), and a wavelength-scanning laser and a photodetector (wavelength interrogation). In many cases, measurement resolution or detection limit is one of the most important performance parameters of the sensors. Intuitively, a high fringe visibility and narrow spectral width of the fringes are favorable to achieving a good resolution regardless of the interrogation method. Many of the reported fiber-optic EFPI sensors are low finesse, using the Fresnel reflections as the mirrors for the FP cavities with spectral fringes being approximately sinusoidal, in which case the spectral width (full width at half-maximum or FWHM) is roughly half of the free-spectral range (FSR) of the FP cavity. To reduce the spectral width of fringes, FP cavity designs with relatively high finesse using coated mirrors have been implemented [10,13,14]. Although FP cavities involving concave mirrors or lenses inside the cavity [15–17], which can account for the diffraction of the beam from the optical fiber, have the potential to achieve the highest finesse, sensors with planar FP cavities [10,18], particularly those formed by metal mirrors, are much easier to fabricate and more forgiving on the selection of the cavity material and the fabrication accuracy. In the past, extensive study has been performed to model and analyze the spectrum of planar FP cavities [19–21]. However, none of them has provided insights on how the sensor parameters affect the measurement resolution, one of the most important performance parameters of the sensors.

In this paper, we present a model to describe a fiber-optic EFPI sensor formed by two planar gold films and analyze the effect of key sensor parameters, including the beam width of the incident light, the metal coating film thickness, the FP cavity length, and the wedge angle of the two mirrors, on the visibility and spectral width of the sensors. Due to its superior performance, wavelength interrogation is employed for the sensor where spectrum is measured by a wavelength-scanning laser, and the wavelength position of a fringe valley is found by polynomial fitting of the data points around the valley. Through Monte Carlo simulations, we have obtained an empirical equation for estimating the wavelength resolution from the fringe visibility and spectral width for a system with a given noise level. The results separate the contributions to the measurement resolution from the system noise and from the sensor structure, which allow us to define a figure-of-merit (FOM) that is

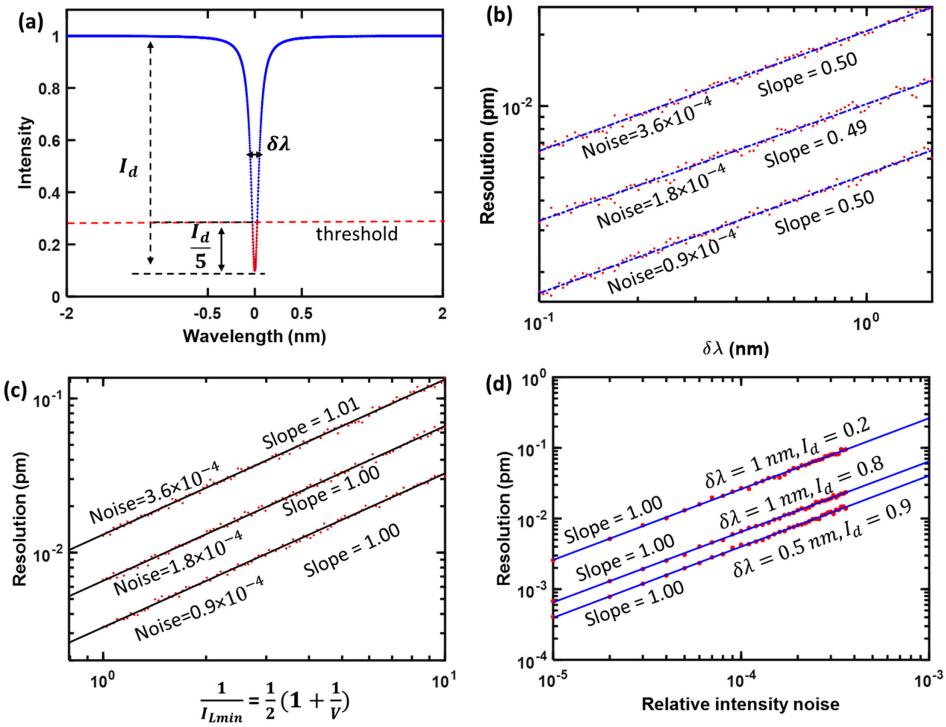

Fig. 1. Analysis of how fringe visibility and bandwidth influences the sensor resolution. (a) Simulated reflection notch of sensor. (b) Sensor wavelength resolution versus 3 dB spectral width ($\delta\lambda$) when the fringe visibility is set at 0.8. (c) Sensor wavelength resolution versus $(1+1/V)/2$ when the 3 dB spectral width is set 0.5 nm. (d) Sensor wavelength resolution versus relative intensity noise.

inherent to the sensor and independent of the system noises. The model provides a useful tool for the design and fabrication of such sensors. In our analysis, metal films are selected as the mirrors for the FP cavity, as opposed to dielectric coatings, with both practical and theoretical considerations. On the practical aspect, dielectric mirrors require complicated mirror design, have more stringent requirements on the coating substrate, are much thicker than metal coatings, and have a higher fabrication cost. On the theoretical aspect, the refractive indices of metals are complex numbers. The model for an FP cavity with metal mirrors is more general with consideration of complex reflection and transmission coefficients of the mirrors and can be easily adapted to analyze an FP cavity with dielectric coatings.

2. WAVELENGTH RESOLUTION OF THE EFPI SENSORS WITH LORENTZIAN LINES

We start with a high-finesse EFPI sensor formed by lossless mirrors, whose reflection spectrum can be approximated by a Lorentzian function (narrow-peak approximation) [22]. Intuitively, the inherent noise performance of the sensor is dependent on the fringe visibility and the spectral width, and a large visibility and a narrower fringe width favor a higher resolution. Analysis of how fringe visibility and width affect the resolution in such a sensor with well-defined spectral shape can provide useful insight on the metal mirrored EFPI sensors with more complex spectral shapes. Figure 1(a) shows a notch in the reflection spectrum, $I_L(\lambda)$, where the maximum reflectivity is normalized to unity, I_d is the depth of the valley related to the fringe visibility of the sensor, $\delta\lambda$ is the 3 dB spectral width counting from the peak to the valley, and λ denotes wavelength. With noise, the measured spectrum is given by

$$I_{rn}(\lambda) = I_L(\lambda) + \delta I, \tag{1}$$

where δI is the intensity noise following the normal distribution arising from the sensor system. In practice, the spectrum is sampled and digitalized. Assume the data points are evenly distributed along the notch at a wavelength interval of 1.2 pm (600 pm over 500 data points). For simplicity, we further assume that the noise of any data point is independent, and the noise level (standard deviation) is uniform for all data points. A second-order polynomial function was applied to fit the data points around the valley to obtain the valley position. The data points were chosen by setting a threshold, and those below the threshold were chosen for curve fitting, as shown in Fig. 1(a). The threshold is defined as the level at one fifth of the peak to valley value ($I_d/5$) above the valley. Monte Carlo simulations were carried out to obtain the standard deviation of the obtained fringe valley position for a given sensor spectrum and noise level, which is defined as the wavelength resolution of the sensor system [23].

We first analyzed the effect of 3 dB spectral width on the sensor resolution. Figure 1(b) shows the sensor resolution as function of the 3 dB spectral width at three different noise levels when the fringe visibility is fixed to 0.8 on the logarithmic scale. The linear fittings of the data points on the logarithmic scale for the three different noise levels show similar slopes close to 0.5, indicating that wavelength resolution is proportional to the square root of the bandwidth $\sqrt{\delta\lambda}$. We then obtained the sensor resolution as a function of valley depth

(I_d) for different noise levels when $\delta\lambda$ was fixed at 0.5 nm, and the result is plotted in Fig. 1(c). The linear fittings of data for the three different noise levels show similar slopes close to one, which reveals that the value of wavelength resolution scales with $1/I_d$. In practice, fringe visibility, V, is more commonly used for characterizing the fringes of an EFPI sensor, and $1/I_d = (1 + 1/V)/2$. Summarizing the results shown in Figs. 1(b) and 1(c), we have found that the sensor resolution is proportional to $\sqrt{\delta\lambda}(1 + \frac{1}{V})$, which can be used as an FOM of the sensor. Figure 1(d) shows the sensor wavelength resolution as a function of noise level with different bandwidths ($\delta\lambda$) and depths (I_d). As expected, the resolution increases linearly with the relative intensity noise with given bandwidth and depth.

It is worth remembering that the results are obtained for high-finesse EFPI sensors whose spectrum can be approximated by Lorentzian functions. The spectrum from EFPI sensors with metal mirrors may be more complex and have large deviations from a Lorentzian shape. Nevertheless, the results indicate that spectral width and fringe visibility are the major parameters that determine the noise performance of an EFPI sensor.

3. OPTICAL MODEL OF THE EFPI SENSORS WITH PLANAR METAL MIRRORS

The fiber-optic EFPI sensor with planar metal mirrors under analysis is schematically shown in Fig. 2. Light from an SMF is expanded by a collimator before illuminating an FP cavity formed by two metal films on both sides of a substrate with thickness of d_3 and refractive index of n_3. In practice, the collimator can be made from a short section of graded-index multimode fiber (GI-MMF) [24], whose refractive index can be considered as a constant, n_1, for the purpose of calculating the reflection and transmission coefficients of the metal film. The thicknesses of the metal films on the front side (M_1) and the far side (M_2) of the substrate are, respectively, d_2 and d_4, and their complex refractive indices are, respectively, n_2 and n_4. For simplicity, we assume the same metals are used for both mirrors, thus $n_2 = n_4$. The external medium surrounding the sensor is assumed to be air with a refractive index of $n_5 \approx 1$.

The light beam at the exit of the collimator can be approximated as a Gaussian beam with a plane wavefront whose electric field is given by $E(\rho) = E_0 \exp(-\rho^2/\omega_0^2)$, where E_0 is the maximum amplitude, ω_0 is the waist radius of the Gaussian beam, and ρ is the radial distance from the center axial of the Gaussian beam. After transmitting through the metal mirror (M_1) into the FP cavity, the electric field of the Gaussian beam travels back and forth between the two mirrors. For each round trip, due to the diffraction of the beam that leads to the mismatch from the original Gaussian field, only a part of the backward traveling light can be coupled into the same mode of the collimator that matches the fundamental mode of the lead-in SMF [19]. The total reflected field coupled into the fundamental mode of the lead-in SMF from the FP cavity is given by

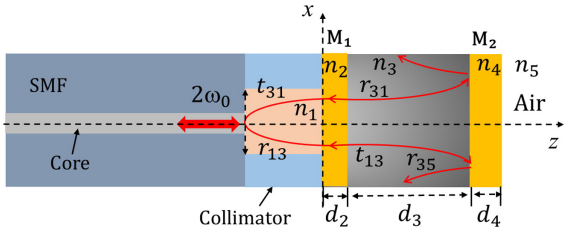

Fig. 2. Schematic of a fiber-optic EFPI sensor with planar metal mirrors.

$$E_r = r_{13}E(\rho) + \sum_{m=2}^{\infty} t_{13}(r_{35})^{m-1}(r_{31})^{m-2}t_{31}\eta_m E(\rho), \quad (2)$$

where r_{13} (r_{31}) and t_{13} (t_{31}) are, respectively, the reflection and transmission coefficients of metal mirror M_1 calculated from the extracavity (intracavity) side of the mirror, r_{35} is the reflection coefficient of mirror M_2 calculated from the intracavity side of the mirror, and η_m is the coupling coefficient of the Gaussian beam after the mth round trip in the cavity to the Gaussian beam of the collimator that matches the fundamental mode of the SMF, which is given by

$$\eta_m = \frac{2}{\omega_0\omega'_m q}\exp[i\phi_m], \quad (3)$$

where ω'_m is the spherical wavefront radius of the Gaussian beam after the mth round trip in the cavity, $\phi_m = k2md_3 - \tan^{-1}(2md_3/z_0)$ is the phase shift due to wave propagation of the Gaussian beam ($z_0 = \pi\omega_0^2 n_3/\lambda_0$ is the Rayleigh range of the beam at free-space wavelength λ_0), and q is a complex number given by $q = \frac{1}{\omega_0^2} + \frac{1}{\omega'^2_m} - i\frac{k}{2R'_m}$, where $k = 2\pi n_3/\lambda_0$ is the wave number, and R'_m is the spherical wavefront radius curvature after the mth round trip in the cavity of the beam. The derivation of Eq. (3) can be found in Supplement 1.

The reflection and transmission coefficients of the metal mirror, M_1, can be deduced using the transfer matrix method [25,26]. The mirror coated on the end of fiber is sandwiched between the collimator and the FPI. Thus, the transfer matrix of this metal layer can be obtained from

$$\begin{bmatrix} M_{11} & M_{12} \\ M_{21} & M_{22} \end{bmatrix} = \frac{1}{t'_{12}}\begin{bmatrix} 1 & r'_{12} \\ r'_{12} & 1 \end{bmatrix}\cdot\begin{bmatrix} \exp(-i\beta_2) & 0 \\ 0 & \exp(i\beta_2) \end{bmatrix} \cdot\frac{1}{t'_{23}}\begin{bmatrix} 1 & r'_{23} \\ r'_{23} & 1 \end{bmatrix}, \quad (4)$$

where $\beta_2 = \frac{2\pi}{\lambda_0}n_2 d_2$, r'_{12}, and r'_{23} are the reflection coefficients defined by the Fresnel reflection arising from the refractive index mismatch of two adjacent layers, the fiber and the metal film, and t'_{12} and t'_{23} are the transmission coefficients. Then, the reflection coefficient r_{13} and transmission coefficient t_{13} of the metal mirror are given by

$$r_{13} = \frac{M_{21}}{M_{11}} = \frac{r'_{12} + r'_{23}\exp(2i\beta_2)}{1 + r'_{12}r'_{23}\exp(2i\beta_2)}, \quad (5)$$

$$t_{13} = \frac{1}{M_{11}} = \frac{t'_{12}t'_{23}\exp(i\beta_2)}{1 + r'_{12}r'_{23}\exp(2i\beta_2).} \quad (6)$$

Using the same method, the other three reflection or transmission coefficients, r_{31}, t_{31}, and r_{35} are obtained and given by

$$r_{31} = \frac{r'_{32} + r'_{21}\exp(2i\beta_2)}{1 + r'_{32}r'_{21}\exp(2i\beta_2)}, \tag{7}$$

$$t_{31} = \frac{t'_{32}t'_{21}\exp(i\beta_2)}{1 + r'_{32}r'_{21}\exp(2i\beta_2)}, \tag{8}$$

$$r_{35} = \frac{r'_{34} + r'_{45}\exp(2i\beta_4)}{1 + r'_{34}r'_{45}\exp(2i\beta_4)}, \tag{9}$$

where $\beta_4 = \frac{2\pi}{\lambda_0} n_4 d_4$. The reflection coefficients and transmission coefficients at the interface of two adjacent layers r'_{lm} and t'_{lm} $(l = 1, \ldots, 5;\ m = 1, \ldots, 5)$ in Eqs. (4)–(9) can be calculated using the Fresnel equations given by

$$r'_{lm} = \frac{n_l - n_m}{n_l + n_m}, \tag{10}$$

$$t'_{lm} = \frac{2n_l}{n_l + n_m.} \tag{11}$$

Substituting Eqs. (3) and (5)–(9) into Eq. (2), the total reflected intensity coupled into the fiber can be obtained by

$$I_{r0} \propto E_r \cdot (E_r)^*, \tag{12}$$

where "*" denotes the complex conjugate.

4. SIMULATION

A. Simulation Methodology

We investigated the noise performance of the sensor system following the method described in Section 2. The reflection fringes in the absence of the noise can be directly obtained by using Eq. (12). A noise term is added to find the wavelength resolution through Monte Carlo simulations.

We validated our model and simulation method by implementing them on a fiber-optic EFPI sensor and comparing its reflection spectrum and noise performance obtained from simulation and experimental measurement. The sensor, which has a structure similar to that shown in Fig. 2, consists of a gold mirrored silicon pillar attached to the end face of a short section of GI-MMF that is connected to a lead-in SMF. The GI-MMF, when its length is controlled, functions as a collimator to expand the light beam guided by the SMF. The fabrication processes are similar to those detailed in Ref. [10] and briefly described as follows. A GI-MMF with a core diameter of 60 μm was spliced to an SMF using a fiber fusion splicer. The GI-MMF was then cleaved to the desirable length using a fiber cleaver with the help of a microscope. Gold coatings were deposited onto both sides of a 100 μm thick silicon wafer by sputtering with estimated coating thickness of 25 nm on the front side (M_1) and 100 nm on the far side (M_2). A small fragment of the coated silicon wafer was glued to the cleaved end of the GI-MMI to complete the fabrication. The red curve in Fig. 3(a) is a single reflection notch of the fabricated silicon EFPI sensor measured by an optical sensing interrogator (Model: sm125, Micron Optics) based on a wavelength-swept fiber laser.

Due to the limited accuracy in characterization and fabrication of the sensor components, fine adjustments of the simulation parameters of the EFPI sensor are necessary to get similar reflection fringes with the fabricated silicon EFPI sensor, including the gold mirror thickness, cavity length, refractive index of silicon, wedge angle, and beam width. Note that the wedge angle refers to the angle formed by the two planar surfaces of the FP cavity (see Section 4.B.3). The parameters used in the simulation are listed in Table 1, and the resulting simulated spectral notch is shown in Fig. 3(a) (blue curve). It is seen that the reflection notches obtained experimentally and from the simulation have similar visibility of 0.46 and similar FWHM of 380 pm.

Table 1. Silicon EFPI Parameters Used in the Simulation

Parameters	$2\omega_0$ (μm)	d_2 (nm)	d_3 (μm)	d_4 (nm)	n_1	n_2	n_3	α (°)
	20	22.5	100	200	1.45	$0.52 + i10.74$	3.4115	0.008

The noise performance of the sensor was studied experimentally and compared with the simulation results. Experimentally, the sensor was placed in the lab environment with a constant temperature, its reflection spectra were obtained continuously using the optical sensing interrogator with a frame rate of 1 Hz, and the wavelength interval between two neighboring data points was 5 pm. For each spectrum, a second-order polynomial function was used to fit the spectrum around a fringe valley and find the wavelength position of the valley. The upper panel of Fig. 3(b) shows the relative fluctuation of the wavelength position for 100 continuous spectral frames obtained from the experiment with a standard deviation of 0.76 pm. For simulation, noise needs to be added to the simulated spectrum of the sensor. With the assumption of an intensity noise with Gaussian distribution, we first needed to determine the standard deviation of the noise used in simulation that should be close to the experimental condition for comparison. Therefore, the fitting errors in the experiment are considered as the relative intensity noise (relative to the intensity of the light at the threshold used for selection of the data for curve fitting) of the system, and its standard deviation is calculated to be 6.1×10^{-3}. In the simulation, independent Gaussian noises with the same standard deviation were added to each data point in each of the spectral frames. After a spectral valley with noise was obtained, polynomial curve fitting was used to find the wavelength position of the fringe valley. The lower panel of Fig. 3(b) shows the relative wavelength obtained from a simulation of 100 iterations. The standard deviation of the result is 0.80 pm, which agrees well with the experimental results (0.76 versus 0.80 pm). The reasonably good agreement between the experimental and simulation results validates the theoretical model and simulation methodology.

B. Simulation Results and Discussion

As shown in Section 2, the resolution is largely determined by the fringe visibility and spectral width of the fiber-optic EPFI sensor. These characteristics are affected by sensor structural parameters such as the thickness of the front gold mirror (d_2), beam width ($2\omega_0$), cavity length (d_3), and wedge angle (θ). In this subsection, we systematically investigate effects of these

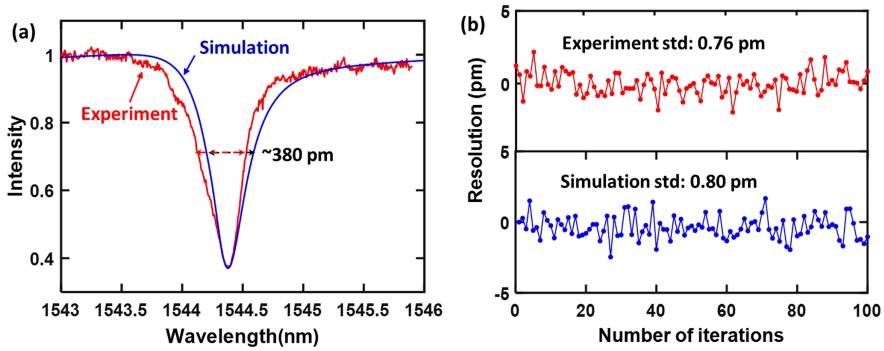

Fig. 3. (a) Reflection spectral notch of a sensor obtained from the experiment (red) and from the simulation (blue). (b) Standard deviation of the fringe valley position (wavelength resolution) of the sensor obtained from the experiment (upper) and the simulation (lower). Std, standard deviation.

parameters on the spectral characteristics and measurement resolution of the sensor by using the Monte Carlo simulation method with a given relative intensity noise of 1.8×10^{-4}. In the simulation, the data points are evenly distributed along the fringes with a separate distance of 1.2 pm.

1. Beam Width and Thickness of the Front Gold Mirror

We first study the influence of the beam width of the illuminating light on the reflection spectrum of the sensor. We use a silicon EFPI sensor with a cavity length of 100 μm and a gold film thickness of 30 nm for the front mirror as an example (the thickness of the back gold mirror is kept at 200 nm throughout the simulation). Figure 4(a) shows the simulated fringes obtained when the sensor is illuminated by Gaussian beams of different beam widths. When the beam width is small (e.g., 10 μm corresponding to a beam width of the mode in a regular SMF), the reflection spectrum shows a relatively broad and shallow notch, partially due to the diffraction of the beam inside the cavity that reduces both the finesse and the fringe visibility of the FPI. As the beam width increases, the diffraction is reduced, leading to higher finesse and increased visibility. It is seen that as the beam width is larger than ~60 μm, the spectral shape of the FPI shows few changes with the beam width, indicating that the diffraction due to the finite beam width can be ignored, and the spectral width and visibility approaches the case where the FPI is illuminated by a plane wave.

Next, we study the effect of the gold film thickness of the front mirror on the reflection spectrum of the sensor with a 100 μm silicon cavity length. We demonstrate how the film thickness affects the shape of the sensor spectrum. For this purpose, we simulate the reflection spectrum of sensors with different gold film thicknesses, as shown in Fig. 4(b), assuming that they are probed by a laser with a beam width of 60 μm, which, as discussed above, is sufficiently large to ignore the diffraction of the laser inside the cavity. It shows that both the spectral width and the visibility of the fringes are sensitive to the film thickness. Specifically, the spectral width seems to monotonically decrease as the film thickness increases, whereas the fringe visibility reaches its maximum value close to unity at a specific film thickness around 20 nm. These observations are confirmed in Figs. 4(c) and 4(d) that show, respectively, the spectral width and fringe visibility as a function of film thickness probed with lasers of different beam widths. Again, the results show that when the beam width reaches ~60 μm, the spectral characteristics are largely independent of the beam width. It is also noted that, from Fig. 4(c), larger gold film thickness results in narrower spectral width of the fringes. This is reasonable because larger gold film thickness yields a higher reflection and better energy confinement of the light field inside the cavity for a narrower resonant notch. However, the larger gold film thickness also results in a larger transmission loss of the front mirror, and, toward the thick gold film end, causing low visibility due to the large mismatch between the beam powers directly reflected from the front mirror and the beam that is transmitted back to the fiber through the film.

It is intuitive that a narrower spectral width and a larger visibility will, in general, favor a better measurement resolution. We use the Monte Carlo simulation to find how the gold film thickness and beam width affect the measurement resolution for the silicon FP interferometer (FPI) sensor with the same cavity length of 100 μm at a given noise level. As an example, we assume that the sensor system noises are white Gaussian noises. Figure 4(e) shows the simulated wavelength resolution as a function of the gold film thickness when the beam widths are 10, 20, 40, 60, and 80 μm. It is seen that the changes of resolution with different beam widths follow a similar trend in the sense that an optimized gold film thickness is found that results in the highest resolution (the value for the resolution is minimum) for a given beam width. When the beam width is larger than 60 μm, the resolution versus metal film curves largely overlap, which is another indication that the diffraction due to the finite beam width becomes negligible. In this case, the optimal thickness for the gold film is ~23 nm. When the beam width is smaller, the highest resolution occurs at a thinner thickness of gold film. For example, when the beam width is 20 μm, the optimal thickness of the gold film is ~12 nm. In general, a larger beam width favors a higher resolution. It is worth noting that when the beam width is 40 μm, the sensor achieves similar resolution as the cases where the beam widths are larger (60 and 80 μm), until the gold film thickness reaches its optimal value around 20 nm. However, as the gold film thickness continues to increase from its optimal value, the resolution for the 40 μm beam width starts to get lower than for the cases of 60 and 80 μm beam widths.

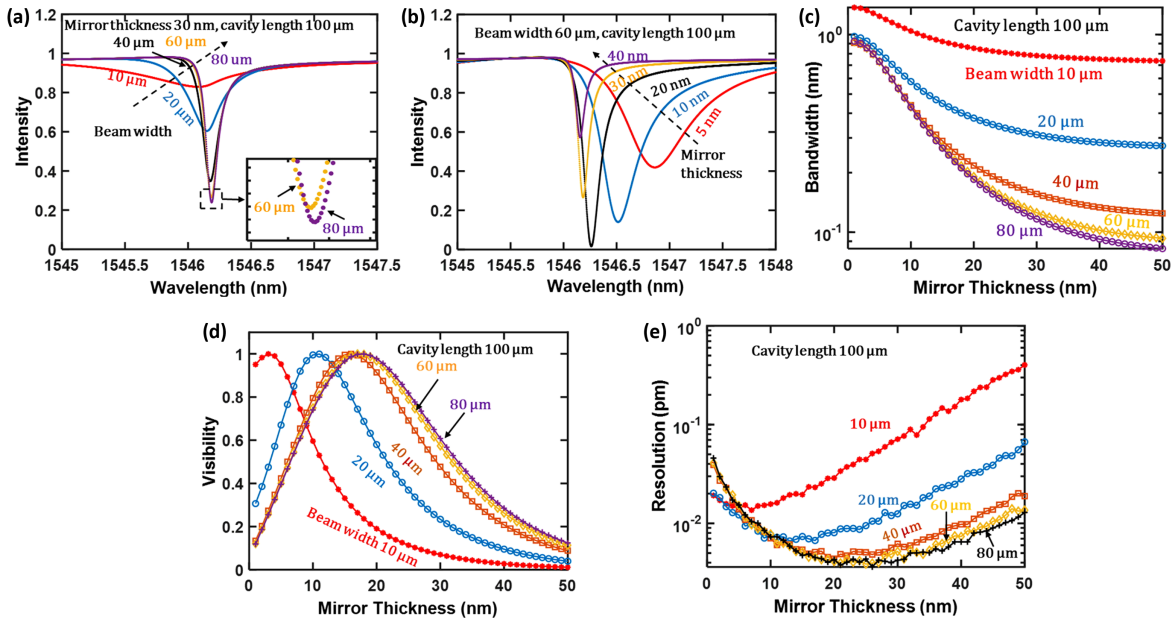

Fig. 4. Effect of the front gold mirror thickness and illuminating light beam width on the visibility, bandwidth, and resolution of the EFPI sensor. (a) and (b), respectively, show the beam width and mirror thickness influence on the reflection spectrum of sensor. (c) shows the sensor bandwidth, (d) visibility, and (e) resolution as function of mirror thickness with different beam widths.

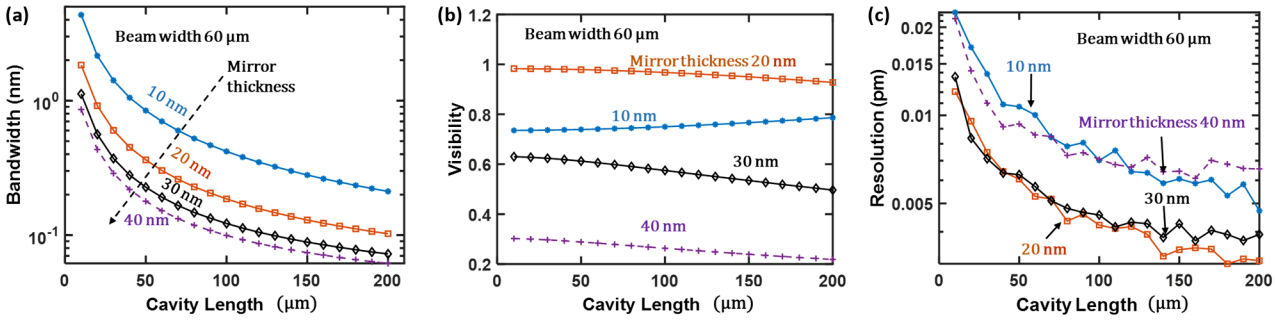

Fig. 5. (a) Sensor bandwidth, (b) visibility, and (c) resolution as function of cavity length with different mirror thicknesses.

2. *Cavity Length*

We then characterized the effect of the length of the FP cavity on the fringe visibility, spectral widths of the fringes, and the wavelength resolution of the sensor system. We set the beam widths to be 60 μm, for which case the beam diffraction can be ignored for a cavity length of 100 μm, as discussed in Section 4.B.1. Figure 5(a) shows the FWHM width of the reflection spectral fringes as a function of the silicon cavity length for different gold film thicknesses. The spectral width monotonically decreases as the cavity length increases, which is expected because the FSR is inversely proportional to the cavity length. As discussed in Section 4.B.1, a thicker gold film always leads to a narrower spectral notch at a given cavity length. Figure 5(b) shows the fringe visibility as a function of cavity length for different gold film thicknesses. In general, the visibility does not vary significantly over the range of simulation (10–200 μm). For a 10 nm thick gold film, the visibility shows a slight increase with the cavity length, while for other thicknesses of simulation, the visibility decreases slightly with the cavity length. When the gold film thickness is 20 nm, the visibility is > 95% over the cavity length range. Figure 5(c) shows the wavelength resolution as a function of cavity length, assuming the same noise characteristics as used in Section 4.B.1. It is seen that the case of the 20 nm gold film thickness has a similar resolution with the case of the 30 nm gold film thickness for the cavity length below 110 μm. With increase of the cavity length (>110 μm), the values of the wavelength resolution of the sensor with the 30 nm gold film become larger than that with the 20 nm gold film. Again, the wavelength resolution is dependent on both the spectral width and the visibility of fringes, and a narrower spectral width and higher visibility favor a higher resolution. As shown in Figs. 5(a) and 5(b), for the case of 20 nm gold film thickness, the spectral width continuously decreases as the cavity length increases and is approximately inversely proportional to the cavity length, so the visibility shows an approximately linear decrease with the cavity length. Compared with the visibility of the 20 nm gold film, the 30 nm film shows a larger decrease of visibility. In addition to the cases of 20 nm and 30 nm gold film thickness, similar variation happens to the cases of 10 nm and 40 nm gold film thicknesses, as shown in Fig. 5(c). We also noticed small fluctuations in Fig. 5(c), which are attributed to the variations

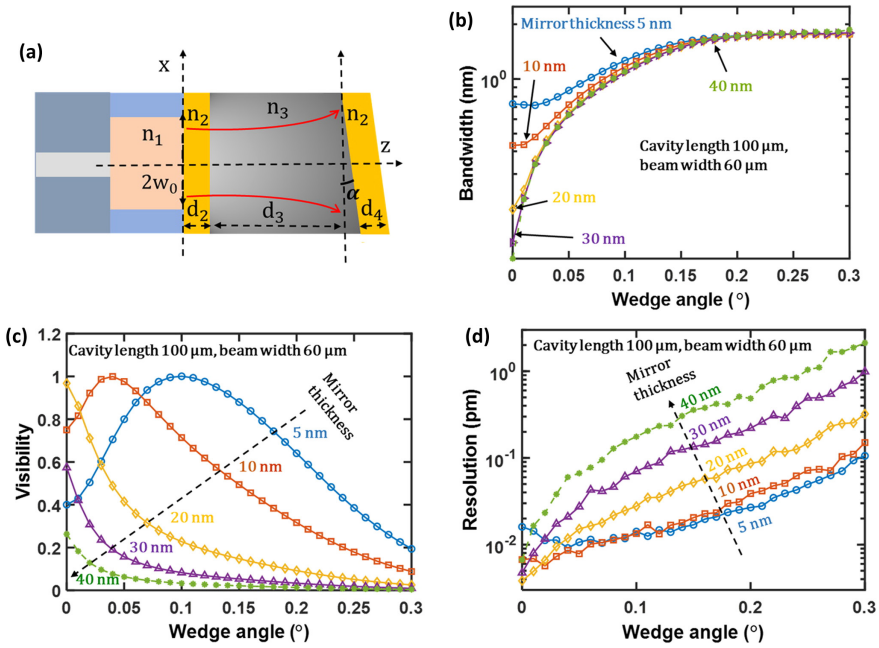

Fig. 6. Wedge angle influences on the sensor visibility, bandwidth, and resolution with different front mirror thickness. (a) Schematic of a fiber-optic EFPI sensor with the two gold mirrors forming a wedge angle. (b)–(d) show the sensor (b) bandwidth, (c) visibility, and (d) resolution as function of wedge angle for different thicknesses of the front gold mirror.

of the pixel distribution relative to the fringe valley position. Measurement resolution decreases monotonically as the cavity length increases. In practical applications, the maximum cavity length is limited by many factors such as required spatial resolution, required sensor size, and fabrication capability. The simulation has a maximum length of 200 μm for the silicon FP cavity, corresponding to an optical length of almost 700 μm, which is above the typical cavity length used for a fiber-optic EPFI sensor.

3. Wedge Angle

In practice, due to the limited fabrication accuracy, the two surfaces of the FPI may not be perfectly parallel, and they may form a wedge angle. It is important to understand the effect of the deviation from the ideal parallelism on the sensor performance. As shown in Fig. 6(a), we assume that the front mirror is perpendicular to the fiber axis (z axis) of the lead-in fiber, and the mirror at the far end has an angle of α with respect to the x axis. The wedge results in a lateral and angle mismatch between the intracavity light beam and the optical mode of the fiber at the coupling plane. For the light beam after m round trips in the cavity, the angle and lateral mismatch are $\theta_m = 2m\alpha$ and $d_m = 2m^2 d_3\alpha$ [27], respectively, and the coupling coefficient is given by

$$\eta_m = \frac{2}{\omega_0\omega'_m q} e^{-p d_m^2\left(1-\frac{p}{q}\right)} e^{-\frac{k^2\theta_m^2}{4q}} e^{-ikd_m\theta_m\left(1-\frac{p}{q}\right)} e^{i\phi_m}, \quad \textbf{(13)}$$

where $p = q - 1/\omega_0^2$, and $\phi_m = k2md_3 - \tan^{-1}(2mD/z_0)$ is the phase due to wave propagation. The derivation of Eq. (13) can be found in Supplement 1. Substituting η_m into Eq. (2) and using Eq. (12), the reflection spectrum of the sensor is obtained.

In the simulation, we assume that the beam width is 60 μm, and the cavity length is 100 μm. Figure 6(b) shows the spectral width of the fringes as a function of the wedge angle in the range of 0–0.3° for different gold film thicknesses. For larger thicknesses (>30 nm) of the gold film, the spectral width increases rapidly with the wedge angle when the wedge angle is less than 0.2°. For smaller thicknesses of the gold film, the spectral width shows little increase with the wedge angle for small wedge angles and large changes when the wedge angle becomes larger (<0.2°). When the wedge angle is increased to 0.2° or larger, the spectral width is independent of the film thickness. The effect of the wedge angle on the fringe visibility is also dependent on the gold film thickness, as shown in Fig. 6(c). For larger thicknesses (≥20 nm), the fringe visibility monotonically decreases as the wedge angle increases. For smaller film thicknesses, as the wedge angle increases, the fringe visibility increases first, reaches its maximum value, then starts to decrease. This behavior is expected because a very thin gold film for the front mirror has a smaller reflection compared with the thick gold film for the back mirror. As the wedge angle increases, it reduces the coupling efficiency of the light reflected from the back mirror to the fiber, and the light beams coupled back to the fiber from both mirrors become more balanced, resulting in a larger visibility. The visibility reaches its maximum value when the two beams are balanced and starts to decrease as the wedge angle continues to increase when the beam coupled to the fiber from the back mirror is weaker than from the front mirror. The simulated wavelength resolution as a function of wedge angle is shown in Fig. 6(d) using the same noise characteristics as discussed in Section 4.B.1. For large gold film thickness (≥20 nm), the value of the wavelength resolution rapidly increases as the wedge angle increases. For example, the resolutions are worsened by more than 10 times when the wedge increases to 0.2° from 0

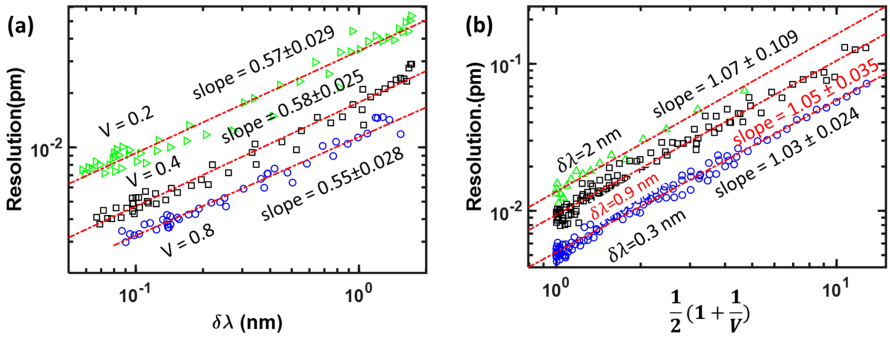

Fig. 7. (a) Sensor resolution versus spectral width of the reflection notches with different fringe visibilities. (b) Sensor resolution variation as function of visibility with different bandwidths.

for all three cases with gold film thickness ≥20 nm. For the two small gold film thicknesses (5 and 10 nm), as the wedge angle increases, the value of wavelength resolution decreases initially due to the increased fringe visibility before reaching its minimum value and starting to increase.

C. Resolution Estimation

The above analysis shows that the suite of sensor structural parameters including the gold film thickness, cavity length, and wedge angles, as well as the beam size of the interrogation light, have a compounding effect on the spectral shapes and wave resolution of the sensors. It is challenging to analytically relate the structural parameters to the resolution performance of sensors. Enlightened by the analysis and results obtained for sensors with simple Lorentzian spectral shapes in Section 2, we can obtain an empirical equation relating these two spectral parameters with wavelength resolution, which will provide a valuable guideline in the sensor design. Toward this end, we analyze the simulation results obtained in Section 4.B to relate the wavelength resolution with the spectral width and fringe visibility at a given noise level without considering the sensor structures and beam size of the probe light. First, we group the data according to the fringe visibility, which allows us to plot the resolution as a function of $\delta\lambda$ at different levels of fringe visibility on the logarithmic scale, as shown in Fig. 7(a). The linear fittings of the data for the three different fringe visibilities show similar slopes close to an average of 0.57. Similarly, we group the data according to the spectral width and scales with $(1+1/V)/2$ for a given spectral width, as shown in Fig. 7(b).

Combining the observations above, we obtain an empirical equation for estimating the wavelength resolution from the fringe visibility and the spectral width of the reflection fringes:

$$\mathrm{Res} = \gamma \frac{\sqrt[0.57]{\delta\lambda}}{2}\left(1+\frac{1}{V}\right), \tag{14}$$

where γ is a coefficient determined by the noise level. This empirical equation separates the contributions to the sensor resolution from the system noise (γ) and from the sensor itself [$\sqrt[0.57]{\delta\lambda}(1+1/V)/2$]. As a result, we can use $\sqrt[0.57]{\delta\lambda}(1+1/V)/2$ as an FOM for the sensor, which is inherent to the sensor and independent of the system noise. To test the validity of the empirical function, we obtained a set of spectral frames with different combinations of spectral width, and the fringe visibility randomly adjusted the parameters of the sensor. We then obtained the wavelength resolution of the sensor through Monte Carlo simulations for two different noise levels, which is plotted against $\sqrt[0.57]{\delta\lambda}(1+1/V)/2$, as shown in Fig. 8. It is seen that the data points form two clusters according to the noise level and, for each cluster, the data points are distributed along a line, indicating the reliability of the empirical equation in predicting the noise performance of the sensor from the spectral width and the visibility of its reflection fringes.

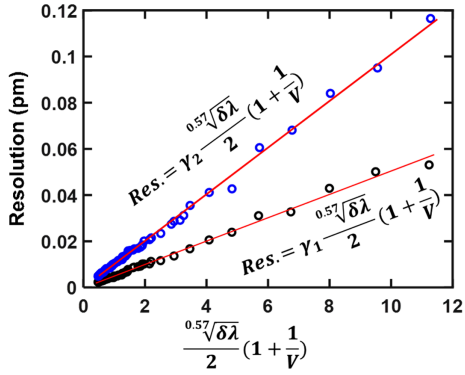

Fig. 8. Simulated sensor resolution versus $\sqrt[0.57]{\delta\lambda}(1+1/V)/2$ for two different noise levels.

5. CONCLUSION

We presented a model to study the noise performance of fiber-optic EFPI sensors with planar metal mirrors. In this model, we assumed that the sensor is operated in a white noise limited regime, and the wavelength interrogation method is applied for the sensor demodulation. To validate our model and simulation method, we use a metal mirrored silicon EFPI sensor as an example. The simulation and experimental results of the silicon EFPI sensor agree with each other reasonably well, indicating the validity of the simulation model in the analysis of the noise performance of the EFPI sensor with metal mirrors. Taking advantage of this model, we theoretically studied the effects of key parameters of the FP cavity, including the metal mirror thickness, beam width, cavity length, and wedge angle, on the sensor noise performance. Based on the simulation results, we find that the wavelength resolution of the EFPI sensor is highly

dependent on the visibility and bandwidth of the reflection fringes. We propose an empirical equation for estimating the noise of the sensor system and a formula involving visibility and bandwidth of the reflection notches that can be used as the FOM to characterize the inherent sensor noise performance. Our work provides a useful tool for designing, constructing, and interrogating fiber-optic EFPI sensors with metal mirrors.

Funding. National Science Foundation (1918074); Office of Naval Research (N000142012562).

Disclosures. The authors declare no conflicts of interest.

Data Availability. Data underlying the results presented in this paper are not publicly available at this time but may be obtained from the authors upon reasonable request.

Supplemental document. See Supplement 1 for supporting content.

REFERENCES

1. G. Liu, M. Han, and W. Hou, "High-resolution and fast-response fiber-optic temperature using silicon Fabry–Perot cavity," Opt. Express **23**, 7237–7247 (2015).
2. W. Tsai and C. Lin, "A novel structure for the intrinsic Fabry–Perot fiber-optic temperature sensor," J. Lightwave Technol. **19**, 682–686 (2001).
3. R. Rong, H. Sun, X. Qiao, J. Zhang, M. Hu, and Z. Feng, "A miniature fiber-optic temperature sensor based on a Fabry–Perot interferometer," J. Opt. **14**, 045002 (2012).
4. Q. Yu and X. Zhou, "Pressure sensor based on the fiber-optic extrinsic Fabry–Perot interferometer," Photon. Sens. **1**, 72–83 (2011).
5. J. Alcoz, C. Lee, and H. Taylor, "Embedded fiber-optic Fabry–Perot ultrasound sensor," IEEE Trans. Ultrason. Ferroelectr. Freq. Control **37**, 302–306 (1990).
6. W. Zhang, R. Wang, Q. Rong, X. Qiao, T. Guo, Z. Shao, J. Li, and W. Ma, "An optical fiber Fabry–Perot interferometric sensor based on functionalized diaphragm for ultrasound detection and imaging," IEEE Photon. J. **9**, 7103208 (2017).
7. G. Liu, Q. Sheng, W. Hou, and M. Han, "Optical fiber vector flow sensor based on a silicon Fabry–Perot interferometer array," Opt. Lett. **41**, 4629–4632 (2016).
8. W. Hou, G. Liu, and M. Han, "A novel, high-resolution, high-speed fiber-optic temperature sensor for oceanographic applications," in *Proceedings of the IEEE/OES 11th Current, Waves and Turbulence Measurement Conference (CWTM)* (2015).
9. Z. Ran, Y. Rao, J. Zhang, Z. Liu, and B. Xu, "A miniature fiber-optic refractive-index sensor based on laser-machined Fabry–Perot interferometer tip," J. Lightwave Technol. **27**, 5426–5429 (2009).
10. Q. Sheng, G. Liu, M. Reinke, and M. Han, "A fiber-optic bolometer based on a high finesse silicon Fabry–Perot interferometer," Rev. Sci. Instrum. **89**, 065002 (2018).
11. T. Zhang, S. Talla, Z. Gong, S. Karandikar, K. Giorno, and L. Que, "Biochemical sensing with a polymer-based micromachined Fabry–Perot sensor," Opt. Express **18**, 18394–18400 (2010).
12. Y. Zhao, X. Hu, S. Hu, and Y. Peng, "Applications of fiber-optic biochemical sensor in microfluidic chips: a review," Biosens. Bioelectron. **166**, 112447 (2020).
13. C. Lee, W. Gibler, R. Atkins, and H. Taylor, "In-line fiber Fabry–Perot interferometer with high-reflectance internal mirrors," J. Lightwave Technol. **10**, 1376–1379 (1992).
14. Y. Jiang and C. Tang, "High-finesse micro-lens fiber-optic extrinsic Fabry–Perot interferometric sensors," Smart Mater. Struct. **17**, 055013 (2008).
15. Y. Sabry, D. Khalil, B. Saadany, and T. Bourouina, "In-plane external fiber Fabry–Perot cavity comprising silicon micromachined concave mirror," J. Micro/Nanolith. MEMS MOEMS **13**, 011110 (2013).
16. D. Hunger, T. Steinmetz, Y. Colombe, C. Deutsch, T. Hänsch, and J. Reichel, "A fiber Fabry–Perot cavity with high finesse," New J. Phys. **12**, 065038 (2010).
17. J. Guggenheim, J. Li, T. Allen, R. Colchester, S. Noimark, O. Ogunlade, I. Parkin, I. Papakonstantinou, A. Desjardins, E. Zhang, and P. Beard, "Ultrasensitive plano-concave optical microresonators for ultrasound sensing," Nat. Photonics **11**, 714–719 (2017).
18. P. Morris, P. Beard, and A. Hurrell, "Development of a 50mhz optical fibre hydrophone for the characterisation of medical ultrasound fields," in *Proceedings, IEEE Ultrasonics Symposium* (2005), pp. 1747–1750.
19. O. Kilic, M. Digonnet, G. Kino, and O. Solgaard, "Asymmetrical spectral response in fiber Fabry–Perot interferometers," J. Lightwave Technol. **27**, 5648–5656 (2009).
20. B. Yu, A. Wang, and G. Pickrell, "Analysis of fiber Fabry–Pérot interferometric sensors using low-coherence light sources," J. Lightwave Technol. **24**, 1758–1767 (2006).
21. P. Wilkinson and J. Pratt, "Analytical model for low finesse, external cavity, fiber Fabry–Perot interferometers including multiple reflections and angular misalignment," Appl. Opt. **50**, 4671–4680 (2011).
22. L. Sanchez-Soto, J. Monzon, and G. Leuchs, "The many facets of Fabry–Perot," Eur. J. Phys. **37**, 064001 (2016).
23. N. Tran, C. Campbell, and F. Shi, "Study of particle size effects on an optical fiber sensor response examined with Monte Carlo simulation," Appl. Opt. **45**, 7557–7566 (2006).
24. Y. Zhang, Y. Li, T. Wei, X. Lan, Y. Huang, G. Chen, and H. Xiao, "Fringe visibility enhanced extrinsic Fabry–Perot interferometer using a graded index fiber collimator," IEEE Photon. J. **2**, 469–481 (2010).
25. M. Born and E. Wolf, *Principles of Optics*, 6th ed. (Pergamon, 1980), Chap. 1.
26. M. Born and E. Wolf, *Principles of Optics*, 6th ed. (Pergamon, 1980), Chap. 13.
27. K. K. Chin, Y. Sun, G. Feng, G. E. Georgiou, K. Guo, E. Niver, H. Roman, and K. Noe, "Fabry–Perot diaphragm fiber-optic sensor," Appl. Opt. **46**, 7614–7619 (2007).